Ocean Engineering 258 (2022) 111813

Contents lists available at ScienceDirect

Ocean Engineering

journal homepage: www.elsevier.com/locate/oceaneng

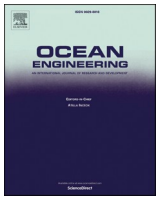

Hydrodynamic performance of a mono-tangent backward-rotating impeller based on tidal current energy utilization

Zhen-hai Wu, Qing Xu, Chang-ming Ling *, Chang-qin Wu

School of Mechanical and Power Engineering, Guangdong Ocean University, Zhanjiang, 524000, China

ARTICLE INFO

Keywords:
Cross-interface
Mono-tangent
Backward-rotating impeller
CFD
Coefficient of power

ABSTRACT

Owing to the continuous consumption of fossil fuel and increasing environmental problems, there is an urgent need to develop technologies for the efficient use of clean energy. In this study, a mono-tangent backward-rotating impeller based on tidal current energy utilization is proposed, and its hydrodynamic performance was studied using the computational fluid dynamics method by establishing a hydrodynamic model of the backward-rotating impeller. The influences of the number of blades, impeller aspect ratio (λ), and different flow speeds on the coefficient of power (c_p) of the mono-tangent impeller were investigated. The results show that the value of c_p of the mono-tangent impeller with four blades is higher than that of the impellers with two, three, five, and six blades. λ has a significant impact on the backward-rotating impeller, with c_p of the impeller reaching an optimal value when λ = 0.5 and the flow speed is 1.25–1.5 m/s (with a tip speed ratio of 0.6–0.75).

1. Introduction

The depletion of global fossil fuel reserves, coupled with increasing environmental problems, has brought into focus the use of renewable clean energy sources such as wind, solar, and ocean energy (Abdelsalam et al., 2021; Yuan et al., 2020). Tidal current energy is a kind of ocean energy that can be potentially exploited because it is widely distributed and predictable and does alter the natural environment (Zhao et al., 2016; Amy et al., 2017). Tidal current energy turbines comprise the main carrier for utilizing tidal current energy, and raising the efficiency of tidal current energy turbine power generation is the primary research direction at present. There are many kinds of tidal current energy turbine power generation devices. These can mainly be divided into vertical axis tidal current energy turbines and horizontal axis tidal current energy turbines according to their structural forms (Li et al., 2016).

The vertical axis turbine has advantages such as simple design and no need for reversing. At present, many scholars have conducted numerous studies on vertical axis turbines. Salleh and co-workers (Salleh et al., 2021a,b) designed a three-bladed Savonius vertical axis turbine, simulated a low-flow-speed river environment in a wind tunnel, and tested the impact of deflectors and guide plates on the self-starting speed and power performance of two-bladed and three-bladed Savonius turbines under low-water-flow-speed conditions. Their results showed that the guide plates can improve the power performance and self-starting ability of Savonius turbines. Abdolkarim et al. (2020) and Vimal et al. (2017) studied the effect on energy capture efficiency of Savonius turbines with different aspect ratios. Their results showed that the efficiency of capturing energy increases with increasing aspect ratio of <1.8, and the opposite is true for aspect ratio of >1.8. Yao et al. (2019) and Abdul et al. (2013) studied the effects of overlap ratio and clearance rate on the energy capture efficiency of Savonius turbines. The Darrieus tidal current energy turbine is another type of vertical axis turbine. Intizar et al. (2020) studied the effect of a pipeline enhancement system on the overall performance of the Darrieus tidal current energy turbine by using computational fluid dynamics (CFD), and their results showed that the pipeline enhancement system can enhance the performance of the Darrieus tidal current turbine, but this will increase the material cost of the turbine. Sun and Huang (2020) put forward a vertical axis tidal current energy turbine with a superhydrophobic surface and investigated its performance numerically. Their results showed that the turbine with a superhydrophobic surface has a maximum energy efficiency improvement of 16.5% compared to one without a hydrophobic surface. A Savonius turbine is used in wind power generation and hydropower generation. The existing research mainly focuses on shape design and flow field environment simulation to improve the performance and efficiency of the turbine. However, Savonius turbines rely on the torque generated by the resistance difference to rotate the turbine (Maldar et al., 2020). Based on single-phase fluid flow, when a Savonius turbine rotates in one phase, its backward-rotating blades move in the opposite

* Corresponding author.
E-mail address: ling-cm@163.com (C.-m. Ling).

https://doi.org/10.1016/j.oceaneng.2022.111813
Received 26 December 2021; Received in revised form 5 May 2022; Accepted 18 June 2022
Available online 1 July 2022

Symbols

a	Extension distance (m)
c_p	coefficient of power
d	Impeller hub diameter (m)
F	Water impact (N)
g	Acceleration of gravity (m/s^2)
P	Pressure (Pa)
T_0	Torque on impeller (N m)
U	Inflow speed (m/s)
WVF	Volume fraction of water (%)
δ	Blade thickness (m)
β	Volume fraction of fluid
σ_{T_0}	Uncertainty component of torque T_0
σ	synthetic uncertainty
A	Effective swept area of the impeller (m^2)
C_t	coefficient of torque
D	Impeller hub diameter (m)
H	Impeller height (m)
R	Impeller radius (m)
TSR	Tip speed ratio
$\boldsymbol{v}$	Velocity vector (m/s)
ρ	Density (kg/m^3)
λ	Aspect ratio
ω	Impeller rotating speed (rad/s)
σ_ω	Uncertainty component of rotational speed ω
σ_U	Uncertainty component of water velocity U

direction to the water flow direction, resulting in large resistance, which causes the efficiency of the Savonius turbine to be low.

The blade profile structure of horizontal axis tidal current energy turbines is similar to that of horizontal axis wind turbines, so many scholars use blade element momentum (BEM) theory to design the blade profiles (Zhu et al., 2020). For example, El-Shahat et al. (2020) used the BEM model to design a horizontal axis turbine blade profile and compared it with the SERG-Tidal model, and they found that the BEM model is better. In addition, Chen et al. (2020), Ramin et al., (2020) and Wang et al. (2020) also used the BEM model to design the blade profile. In addition to using the BEM model for blade profile design, relevant algorithms are generally needed for optimization. For example, Madhan et al. (2019) used the Kriging model to optimize the cross section of the blade profile and conducted a numerical analysis using CFD. Luo et al. (2014) proposed a multipoint optimization method for the blade profile and used CFD to simulate the performance of the original and optimized blade profiles. The optimized blade profile had better hydrodynamic performance than the original blade profile under all three conditions.

The horizontal axis turbine does work under the partial force of water, and the blades of horizontal axis turbine are shown in Fig. 1. If the force applied to the turbine by the water flow is assumed to be F, the rotation axis of the turbine is parallel to the direction of the water flow, and the rotation direction of the turbine is perpendicular to the direction of the water flow, then each blade has a torsion angle, so it can receive the work done by the water flow. However, the force F cannot fully act on the turbine, and the turbine can only receive the work done by part of the force (i.e., F_2); as a result, not all water flow can do work on the turbine. Additionally, current hydro turbines spin underwater. As the turbine rotates, there is more resistance to the flow of water than it is in the air.

We (Ling et al., 2019a,b; Zhang, 2019) put forward a semi-submersible marine current energy power generation method. This method entails putting half of the impeller in the water and half in the air. As shown on the right in Fig. 1, the lower part of the impeller is immersed in water, facing the direction of water flow, and can receive all the work done by the positive force of water flow, and the impeller rotates backward (hence is also called backward-rotating impeller), making it a vertical axis impeller. During the backward rotation of the impeller, the resistance on the upper half impeller in the air is far less than that on the half in the water, and the loss of the work done by water flow is less, which is conducive to improving the efficiency of marine current energy power generation. Because the rotation axis of the backward-rotating impeller is perpendicular to the direction of water flow, it is a vertical axis turbine. Because there is greater resistance when the impeller enters and exits the water surface, we (Ling et al., 2019a) proposed the concept of arc tangency of the impeller blades. When the arc of the impeller blades is tangent to the water surface, it can ensure that the impeller is perpendicular to the water surface, and the resistance is least when entering and exiting the water surface.

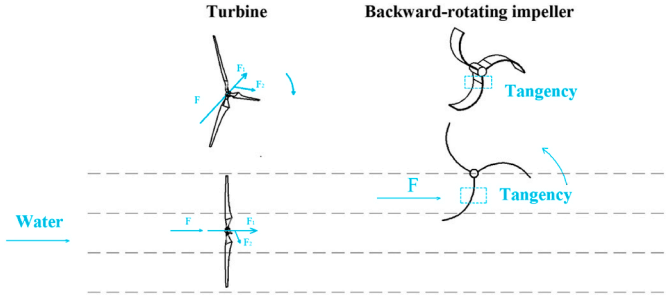

Fig. 1. Comparison between a turbine (left) and a backward-rotating impeller (right).

On the basis of the previous stage, this paper proposes a mono-tangent backward-rotating impeller. For this type of blade arc tangency, only one segment of arc is tangent, so it also known as mono-tangent. Statistics show that the average flow speed of tidal current is ~1–2 m/s in the marine environment (Vogel et al., 2019; Patxi and Yusaku, 2019). Therefore, we use CFD to study the performance of a mono-tangent backward-rotating impeller at this flow speed, and we also analyze the influences of the number of blades and the aspect ratio on the performance of backward-rotating impellers. We used the commercial software ANSYS FLUENT (v20.0) for numerical simulation studies.

2. Mono-tangent backward-rotating impeller model and calculation method

2.1. Analysis of energy characteristics of mono-tangent backward-rotating impeller

The energy obtained by the impeller is shown in Fig. 2, we refer to the mathematical model proposed by Chauvin (Ion et al., 2013).The torque T_0 of the turbine can be calculated by the following formula:

$$T_0 = T_M + T_D \tag{1}$$

The torque of the part driven by the turbine is T_M, which is related to the backward rotating blades. The torque of the drag section of the turbine is T_D, which is related to the return blades.

It is assumed that the differential pressure across the backward rotating blades is ΔP_M and the differential pressure across the returning blades is ΔP_D. The total torque can be expressed as:

$$T_0 = \frac{1}{2}R^2 H \int_0^{\frac{\pi}{2}} (\Delta P_M - \Delta P_D)\sin 2\theta d\theta \tag{2}$$

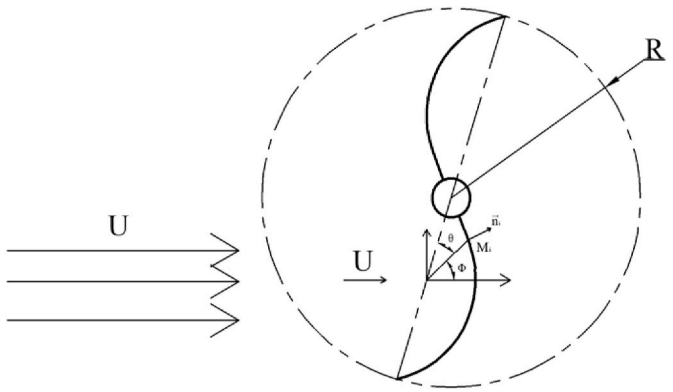

Fig. 2. analysis of energy characteristics of mono-tangent backward-rotating impeller.

The average power $\overline{P_0}$ can then be obtained by integrating the torque from 0 to π.

$$\overline{P_0} = \omega \cdot T_0 = \frac{\omega}{\pi} \int_0^{\pi} T_0 d\Phi \tag{3}$$

To study the performance of the impeller, power normalization coefficient processing was conducted for the power of the impeller as follows:

$$c_p = \frac{\omega T_0}{\frac{1}{2}\rho U^3 A} \tag{4}$$

Where c_p is the coefficient of power,a dimensionless parameter; ω is the impeller rotating speed(in $\frac{\text{rad}}{\text{s}}$);$T_0$ is the torque applied to the impeller (in N · m); ρ is density (in kg/m^3); U is the inflow speed of water (in m/s); and $A = RH$ is the swept area of the impeller (in m^2), where H is the height of the impeller (in meters) and R is the radius of the impeller (in meters).

As can be seen from Eq. (4), the coefficient of power actually indicates the ratio of impeller output power to water flow power. The larger the ratio, the higher the actual output power of the impeller, and thus the higher the water flow energy obtained by the turbine.

The coefficient of torque is defined as follows:

$$C_t = \frac{4T_0}{\rho U^2 R^2 H} \tag{5}$$

The tip speed ratio (TSR) is given by

$$\text{TSR} = \frac{\omega R}{U} \tag{6}$$

As can be seen from Eq. (5), the coefficient of torque actually represents the ratio of the torque received by the impeller to the torque generated by the water flow. The larger the ratio, the higher the actual output torque of the impeller, and thus the higher the water flow energy obtained by the turbine. As can be seen from Eq. (6), TSR represents the ratio of the linear speed of the impeller to the inflow speed of the water flow. The larger the ratio, the higher the actual impeller rotation speed, and thus the higher the water flow energy obtained by the turbine.

The aspect ratio is

$$\lambda = \frac{H}{D} \tag{7}$$

where D is the diameter of the backward-rotating impeller.

2.2. Physical model and mathematical model

A three-dimensional physical model was established according to the working principle of the backward-rotating impeller. As shown in Fig. 3,

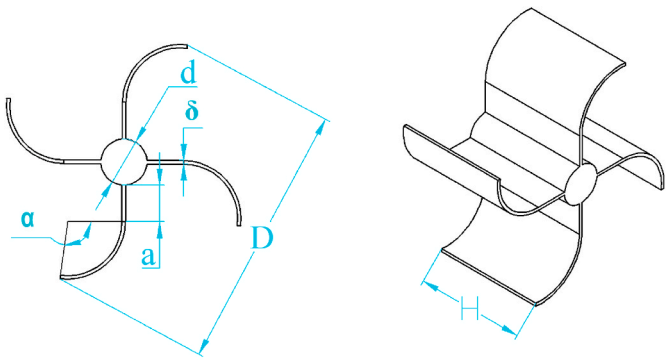

(a) Backward-rotating impeller model

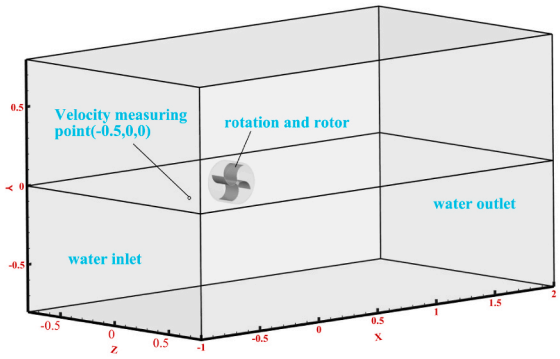

(b) Computational domain model

Fig. 3. Physical model.

the impeller consists of a hub and blade. The hub radius is d, the arc section of the blade is tangent to the extension section, the length of the extension section is a, the arc angle of the arc section is α, the thickness of the blade is δ, and the height of the impeller is H. The impeller model information for the different impeller heights H studied here is given in Table 1. The water flow enters the fluid domain from the inlet boundary to impact the impeller, and the impeller rotates under force.

As shown in Fig. 3(b), in the upper part of the computational domain, the impeller is placed at the interface of the air and water flow. If both water and air are assumed to be homogeneous fluids, the momentum obtained by the turbine through air flow is much smaller than that obtained through water flow; consequently, the influence of air inflow velocity will not be considered. In the calculation, the initial air flow field was in a static state, and it was assumed that the magnitude and direction of water flow speed were both constant. Because there were no internal and external heat sources in the fluid, and the impact of impeller energy loss on water flow temperature was not considered in the calculation process, the fluid temperature difference was ignored in the calculation, and the fluid temperature was considered to be constant. In other words, the fluid energy equation was not solved during the simulation. The numerical model equations are given in the following.

The continuity equation is

$$\frac{\partial \rho}{\partial t} + \nabla \cdot (\rho \mathrm{v}) = 0 \tag{8}$$

The SST k-omega turbulence model proposed by Menter was used as the turbulence simulation model (Menter, 1994) because, in many CFD studies on turbines, this model has been proven to have better flow separation prediction and more accurate performance evaluation (Wang et al., 2012; Ahmed, 2016; Sufian et al., 2017) For the fluid domain, the multiphase volume of fluid (VOF) model was used to track the volume fraction of fluid in the whole fluid domain to simulate the air–water flow state.

Table 1
Impeller model information.

Working condition	Impeller diameter D (m)	Hub diameter d (m)	Extension section a (m)	Arc angle of tangent arc section, α (°)	Blade thickness δ (m)	Impeller height H (m)
1	0.24	0.024	0.02	97	0.002	0.072
2	0.24	0.024	0.02	97	0.002	0.120
3	0.24	0.024	0.02	97	0.002	0.198

The momentum equation based on the multiphase flow VOF model is

$$\frac{\partial}{\partial t}(\rho \mathbf{v}) + \nabla \cdot (\rho \mathbf{v}\mathbf{v}) = -\nabla p + \nabla \cdot \left[\mu\left(\nabla \mathbf{v} + (\nabla \mathbf{v})^{\mathrm{T}}\right)\right] + \rho \mathrm{g} \tag{9}$$

where p is the static pressure, ∇ is the divergence, and $\mathbf{v}$ is the velocity vector.

According to the fluid volume fraction equation, the VOF method was used to track the two-phase interface:

$$\frac{\partial \beta}{\partial t} + \nabla \cdot (\beta \mathbf{v}) = 0 \tag{10}$$

where β is the volume fraction of fluid. When $\beta = 0$, the grid cell has only a gas phase. When $\beta = 1$, the grid cell has only a liquid phase. When $0 < \beta < 1$, the grid cell includes both gas and liquid phases. The physical parameters of the grid cell were calculated through weighted averaging of the volume fraction of fluid:

$$\rho = \beta_l \rho_l + (1 - \beta_l)\rho_g \tag{11}$$

and

$$\mu = \beta_l \mu_l + (1 - \beta_l)\mu_g \tag{12}$$

where the subscripts l and g represent liquid phase and gas phase,

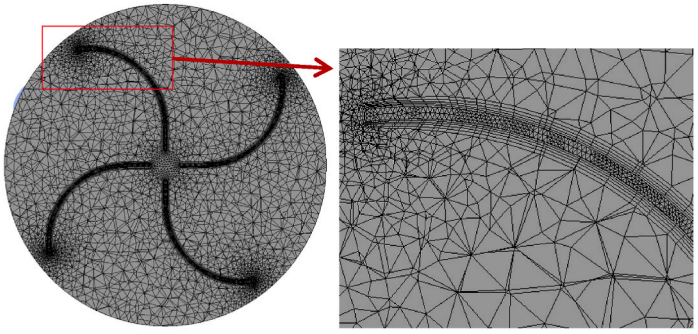

(a) Rotation domain grids

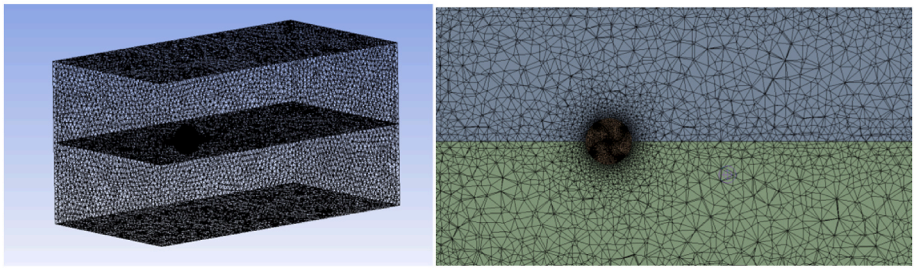

(b) Rotation domain grids

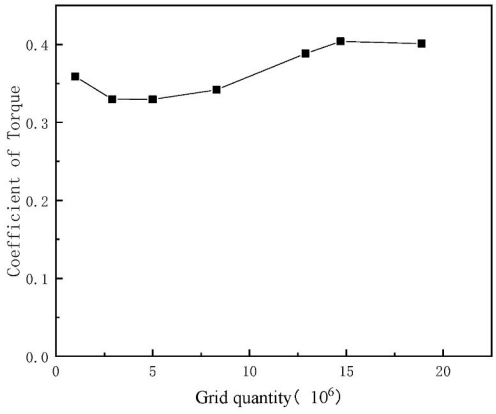

(c) Grid independence assessment

Fig. 4. Rotation domain grids and grid independence assessment.

respectively.

To solve the above model equations, the boundary conditions were set as follows: Except for the water inlet and the water outlet, the others were set as the wall surface.

When solving the above mathematical model equations, the SIPLE algorithm was used to solve for the pressure–velocity coupling, the diffusion term was discretized by using the second-order upwind scheme, the pressure gradient term was discretized by using the PRESTO algorithm, and the unsteady-state term was discretized by using first-order implicit discretization. The six-degree-of-freedom method was used to solve for the motion of the impeller, which was based on the principle of calculating the pressure and shear stress on the impeller surface by numerical integration to solve for the moment applied to the impeller.

2.3. Grid independence verification

The model was divided into unstructured mesh, the rotational domain was densified, and a contact surface was set between the fluid domain and the rotational domain. Boundary layers were set for the impeller wall surface, and the thickness of the first boundary layer was 0.03 mm. For the SST turbulence model, in our study, Y Plus is less than 1. Although there are some reports that less than 15 is acceptable (Ramana and Kishore, 2013; Mohammad et al., 2012).

To ensure that the calculation results were independent of the number of grids, seven groups (The grid numbers of groups 1–7 are 104847, 294226, 501777, 830253, 129770, 1472631, 1899993 respectively.)of grids with different numbers of grids were defined and these seven groups were assessed. The results are shown in Fig. 4. Finally, 129770 grids were chosen for the calculation.

2.4. Experimental scheme design

To verify the performance of the mono-tangent backward-rotating impeller, an experimental platform was designed and built. The experimental platform device is shown in Fig. 5. The experimental platform was connected by two tanks (one at a high position and the other at a low position) and an intermediate water channel. The high-position water tank acted as a water supply pool, with its potential energy being converted into kinetic energy to simulate tidal current impact on an impeller. The water flowed from the water supply pool to the low-position water tank, which served as a water storage pool, through the water turbine, and the water in the low-position water tank was pumped back to the high-position water tank for recycling. The two water tanks were connected by an open channel as the experimental waterway.

An LS300-A self-recording flow meter was used to measure the water flow speed during the experiment. The measurement range of this meter is 0–4 m/s, and the measuring error is <1.5%. The meter has its own portable SD card that can automatically store the data. An experimental noncontact rotating shaft torque measuring instrument was selected to measure the impeller rotation speed and torque. The torque sensor used (HLT-138) had a measuring range of 0–5 N·m and a measuring accuracy of ±0.5%.

3. Results and analysis

3.1. Experimental verification of the simulation method

An experimental method was used to verify the correctness of the numerical method. First, the backward-rotating impeller with $\lambda = 0.5$ was selected for the experiment, and the experimental flow speed was controlled to within 1.0–2.0 m/s. Starting from 1 m/s, the impeller rotating speed and torque were measured every 0.1 m/s. After the flow speed reached 2.0 m/s, it was reduced to 1.0 m/s in turn, and the impeller rotation speed and torque were measured at every 0.1 m/s interval. This procedure was repeated three times, and the average

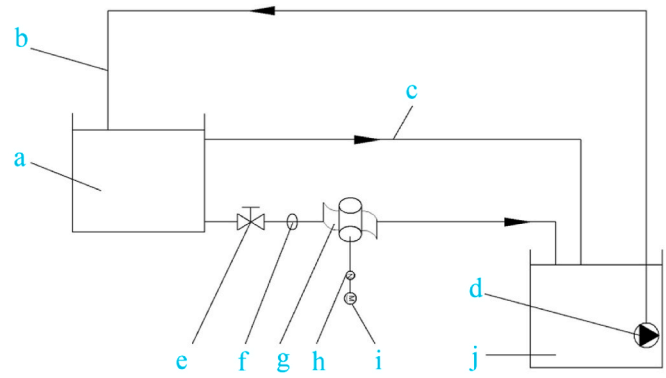

(a) Schematic diagram of the experimental apparatus

(b) Photograph of the experimental apparatus

Fig. 5. Diagram of the experimental apparatus. a: high position water tank; b: circulation pipeline; c: bypass pipeline; d: submerged pump; e: butterfly valve; f: flow meter; g: backward-rotating impeller; h: torque tachometer; i: generator; j: low-position water tank.

values of rotation speed and torque at the same flow speed were taken to calculate the TSR and the coefficient of power (c_p). The comparison between experimental results and simulation results is shown in Fig. 6. The maximum relative error is 9.4%, and the average relative error is 7.4%.

The uncertainty of the experiment is calculated according to the

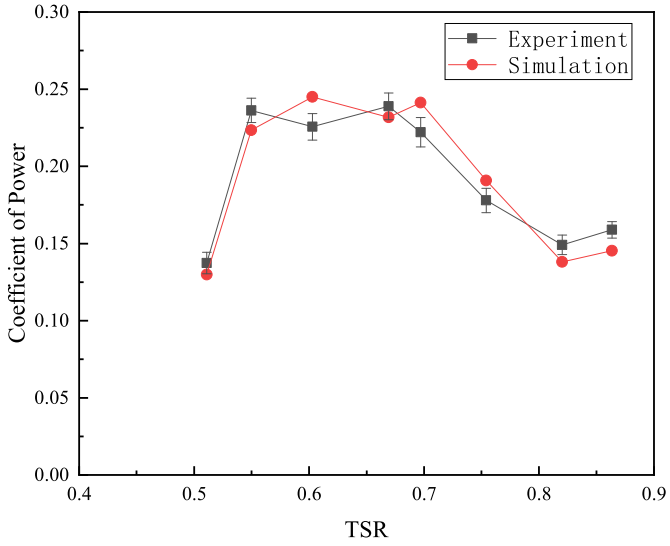

Fig. 6. Coefficient of power of a backward-rotating impeller as a function of TSR when $\lambda = 0.5$.

following formula(Fei, 2015).

Uncertainty component of rotational speed ω:

$$\sigma_\omega = \left|\frac{\partial c_p}{\partial \omega}\right|\alpha_\omega + \left|\frac{\partial c_p}{\partial \omega}\right|\alpha_{ts} \tag{13}$$

3.1.1. Uncertainty component of torque T_0

$$\sigma_{T_0} = \left|\frac{\partial c_p}{\partial T_0}\right|\alpha_{T_0} + \left|\frac{\partial c_p}{\partial T_0}\right|\alpha_{ts} \tag{14}$$

Uncertainty component of water velocity U

$$\sigma_U = \left|\frac{\partial c_p}{\partial U}\right|\alpha_\omega + \left|\frac{\partial c_p}{\partial U}\right|\alpha_{fm} \tag{15}$$

Combination of Uncertainties

$$\sigma = \sqrt{\sigma_\omega^2 + \sigma_{T_0}^2 + \sigma_U^2} \tag{16}$$

Among them, α_ω is the standard deviation of the average value of the rotational speed, α_{T_0} is the standard deviation of the average value of the torque, α_U is the standard deviation of the average value of the water flow velocity, α_{ts} is the standard uncertainty caused by the indication error of the rotational speed and torque measuring instruments, α_{fm} is the standard uncertainty caused by the indication error of the flow rate measuring instrument.

The calculation results of the synthetic uncertainty are shown in Fig. 6.

We summarize the reasons for the deviation of three experiments and simulations. First, due to the short distance between the two tanks, the water flow supplied by the submersible pump is still unstable in the high-position water tank. Unstable water flow impinging on the impeller is one of the reasons for the deviation of the experiment and simulation. Also, the width of the flow channel of the test rig is smaller, which is one reason for the experiments and simulations. Finally, regarding the supporting structure, in our experiments, the ceramic bearing was the supporting structure. In numerical simulations, adding support structures will increase the complexity of the numerical simulation. Therefore, we did not add support structure models. Of course, this creates a bias between experiment and simulation. According to the results of our tests, the data show a consistent trend, so we consider the numerical simulation method acceptable.

3.2. Influence of the number of blades on the impeller

The inlet boundary condition was set to the velocity inlet, and the velocity was set to 1.5 m/s. The simulations were performed for impellers with an aspect ratio of λ = 0.3 and two to six blades, respectively. The impeller coefficient of power obtained is shown in Fig. 7. The impeller coefficient of power with four blades is the highest, followed by the impeller with three blades. Fig. 8 shows the distribution of liquid (water) phase volume fraction (WVF) and pressure distribution of impellers with different numbers of blades. As shown in Fig. 8(a), when the impeller is impacted horizontally by the water flow, the arc shape of the impeller blocks part of the water flow when entering the water, creating resistance. At a certain moment, this resistance forms a force balance with the impact force of the water flow on another arc of the impeller, resulting in no rotation or low-speed rotation; consequently, the output power of the two-bladed impeller is relatively low. As shown in Fig. 8, compared with two blades, when the number of turbine blades increases, the coefficient of power (c_p) correspondingly increases. However, under the working conditions with five and six blades, the phenomenon in which the water flow is blocked by the arc section of blades arises many times because of the increase in number of blades, causing the increase in the resistance to the turbine (Fig. 8(d) and (e)), thereby decreasing the output powers of the impellers with five and six blades. In addition, with the increase in the number of blades, the dead

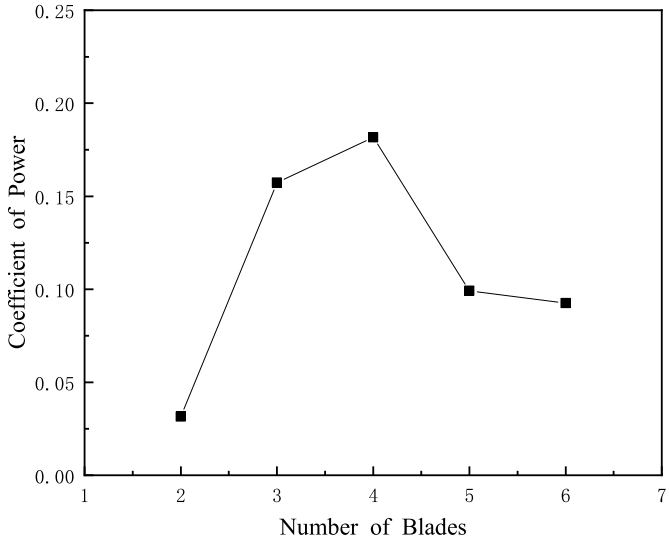

Fig. 7. Coefficient of power (c_p) of impellers with different numbers of blades when λ = 0.3.

weight of the impeller increases, also leading to a decrease in the output power of the impeller.

Fig. 9(a)–9(e) shows diagrams of the distribution of the coefficient of torque of impellers with two to six blades with time, respectively. The coefficient of torque exhibit periodicity. The reason for this is as follows: The impeller rotates after being impacted by the water flow; the blades are resisted when entering the water surface, so the torque gradually decreases; the blades in the water undergo the positive impact force of the water flow, so the torque gradually increases; with the rotation of the impeller, the coefficient of torque changes periodically. The length of the period is related to the number of blades. The more blades there are, the shorter the period of a blade in contact with the water, and thus the shorter the change period of the coefficient of torque. If there are too many blades, the number of times they block the water flow will increase; therefore, the torque on the impeller is much more offset by the resistance on it when it enters the water, and its output power is reduced. Because four blades are symmetrically arranged up and down and left and right, the force on the impeller is relatively uniform, and the simulation result is also the best. Therefore, in all of the subsequent performance analyses, the four-bladed impeller was used as an analysis object for analysis of the performance impact parameters of the backward-rotating impeller.

3.3. Influence of impeller aspect ratio and water flow speed on impeller output power

In this section, the working conditions are set, and the influences of impeller aspect ratio (λ) and water flow speed on impeller output power are discussed and analyzed. Four-bladed impellers with λ of 0.3, 0.5, and 0.8 were selected for numerical simulation studies, and the water flow speeds were set to 1, 1.25, 1.5, 1.75, and 2.0 m/s, respectively. The results are shown in Fig. 10, from which it can be seen that, when λ = 0.3, the value of c_p of the impeller increases with the increase in the water flow speed and finally tends to be stable. When λ = 0.5 and the water flow speed is above 1.25 m/s, the value of c_p decreases with the increase in speed. When λ = 0.8, the decreasing trend of c_p with the increase in water flow speed is more significant. According to Eq. (5), the output power of the impeller is directly proportional to the torque and the rotation speed. If the resistance on the impeller increases, the torque and coefficient of power of the impeller will decrease. When λ increases, the energy of the water flow that can be used will increase, but the resistance on the impeller when entering the water will also increase. Fig. 11(a) and 11(c) show diagrams of the distribution of the impeller

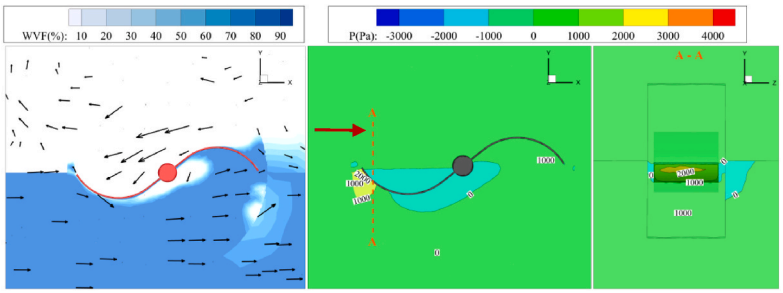

(a) Impeller with two blades

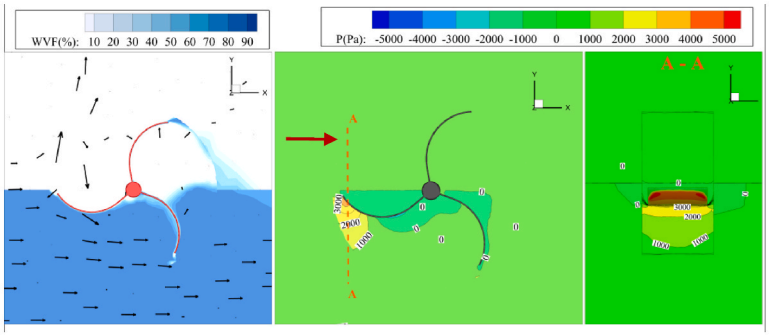

(b) Impeller with three blades

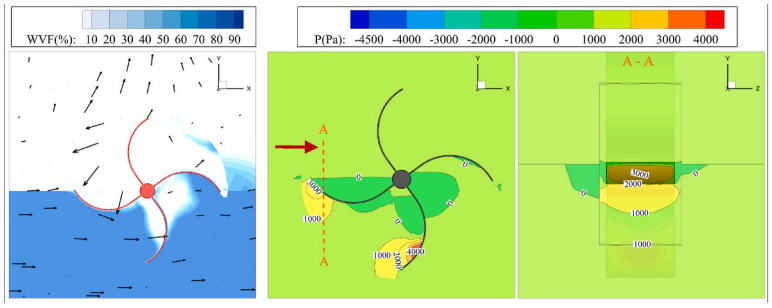

(c) Impeller with four blades

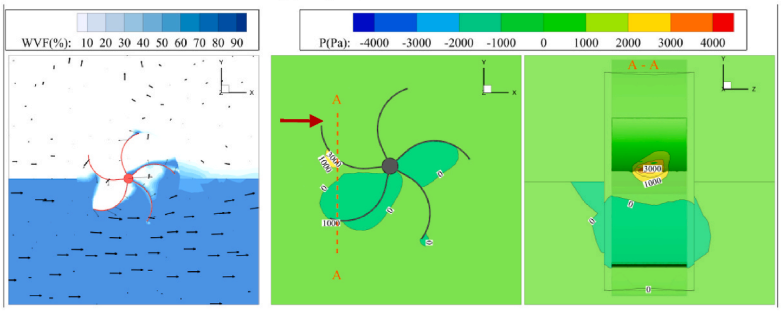

(d) Impeller with five blades

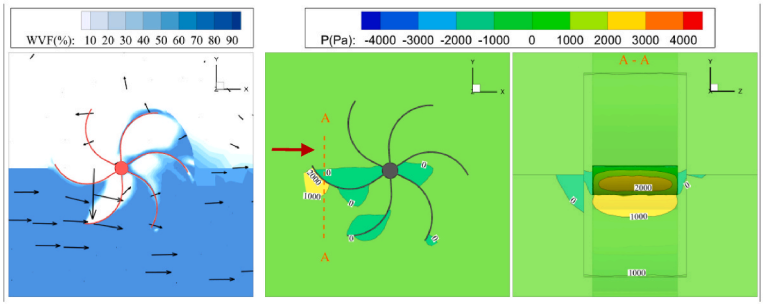

(e) Impeller with six blades

Fig. 8. Distribution of WVF and distribution of pressure (P) on impellers with different numbers of blades with and aspect ratio of $\lambda = 0.3$.

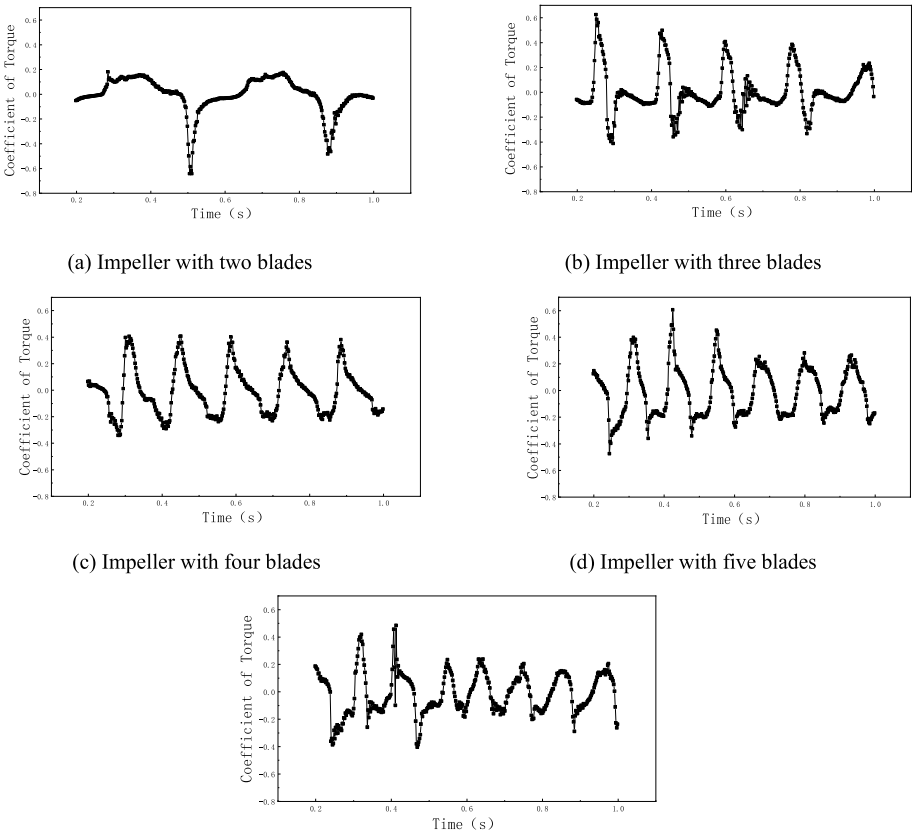

(a) Impeller with two blades

(b) Impeller with three blades

(c) Impeller with four blades

(d) Impeller with five blades

(e) Impeller with six blades

Fig. 9. Distribution of coefficient of torque for impellers with two to six blades with time.

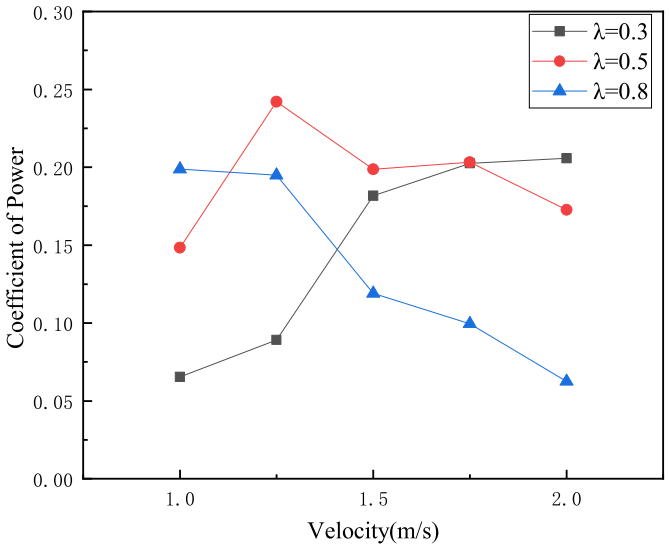

Fig. 10. Variation of the coefficient of power as a function of water flow speed for an impeller with four blades at different aspect ratios.

WVF and the distribution of the pressure (P) on the impeller when λ is 0.3, 0.5, and 0.8, respectively. It can be seen from these figures, coupled with Fig. 10, that, when λ = 0.8, the height of the impeller is the largest, and when the water flow speed increases, the resistance on the blades increases when they enter the water. Therefore, when the water flow speed is 1 m/s, c_p is the largest. Conversely, when the water flow speed is 2 m/s, c_p is instead the lowest. When λ = 0.5, the height of the impeller is appropriate, and the resistance on the impeller is reduced. Therefore, c_p increases with the increase in water flow speed when the water flow speed is < 1.25 m/s, is the largest when the water flow speed is 1.25 m/s, and decreases with the increase in water flow speed when the water flow speed is > 1.25 m/s. When λ = 0.3, the height of the impeller is the smallest and the resistance on the impeller is the lowest, so c_p increases with the increase in water flow speed, and it is the largest when the water flow speed is 2 m/s. The peak value of c_p moves forward with the increase in λ when the water flow speed is 1–2 m/s. When λ is 0.5, the impeller gets the best c_p at a water flow speed of 1.25 m/s.

Fig. 12 shows the relationship between TSR and coefficient of power. When λ = 0.3, the output power of the impeller increases with the increase in TSR and water flow speed. When TSR reaches 0.8–0.9, c_p tends to be stable. When λ = 0.5, c_p first increases and then decreases with the increase in water flow speed and TSR. When the TSR is between 0.55 and 0.7, c_p is the best. When λ = 0.8, c_p increases with the increase in TSR. From Figs. 10–12, it can be seen that the resistance on the impeller with small λ is small because of its short height; therefore, with the increase in water flow speed, TSR increases and c_p also increases. For the impeller with moderate λ, its height is also moderate, and the resistance on it increases slightly at low water flow speed and greatly at high water flow speed, so c_p increases first and then decreases. The impeller with the largest λ receives great resistance at high water flow speed because of its greater height. TSR decreases with the increase in water flow speed, and c_p also decreases with the increase in water flow speed.

4. Conclusions

A mono-tangent backward-rotating impeller is proposed, and a rear-rotating impeller model is established. The hydrodynamic performance of the mono-tangent backward-rotating impeller is studied using CFD

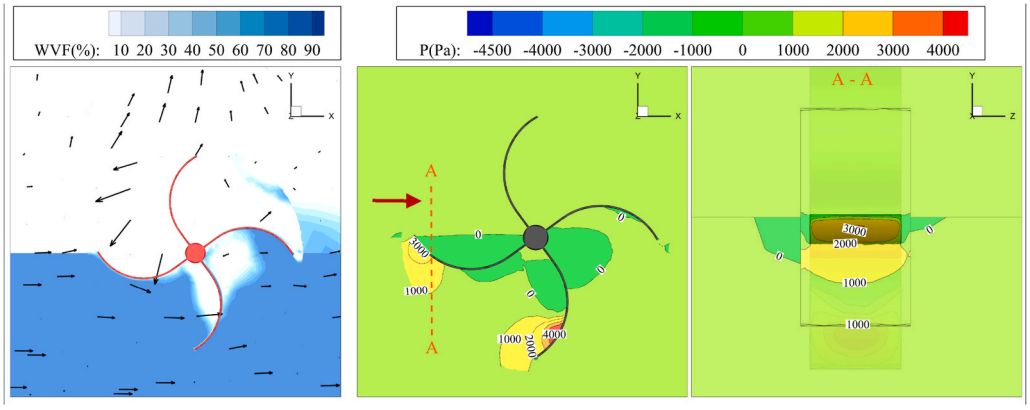

(a) λ = 0.3

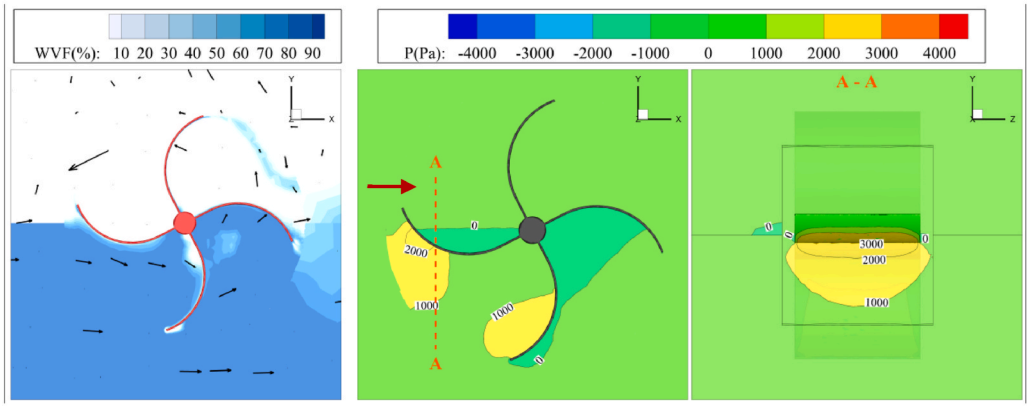

(b) λ = 0.5

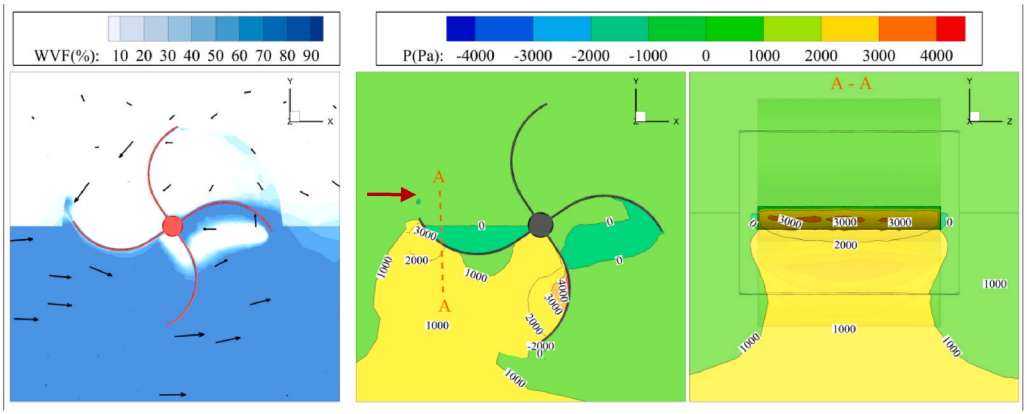

(c) λ = 0.8

Fig. 11. Distribution of WVF and distribution of pressure (P) on an impeller with four blades with different aspect ratios at a water flow speed of 1.5 m/s.

methods, and the following conclusions are reached from the analysis and discussion:

(1) The simulation was experimentally verified, with a maximum relative error of 9.4% and an average relative error of 7.4%. The experimental and simulation results are in good agreement, which verifies the accuracy of the simulation.

(2) Impellers with two to six blades impacted by the water flow were simulated, and the results show that the four-bladed one has a higher value of c_p. The coefficient of torque of the impeller changes periodically, which is related to the number of impeller blades. The balance between the resistance and pushing force on the impeller with two blades when entering the water will lead to a decrease in output power. For impellers with five and six blades, because of the short period and the large number of blades, the resistance on the impeller increases when the impeller enters the water, which leads to a decrease in output torque and output power of the impeller.

(3) The c_p values of four-bladed impellers with different λ values at different inflow speeds were compared, and the results show that the c_p values of impellers with different λ values exhibit different trends when they are impacted by different water flow speeds. When λ = 0.3, the increase in water flow speed will increase the value of c_p of the impeller, but c_p will eventually become stable. When λ = 0.5 and 0.8, the increase in water flow speed will

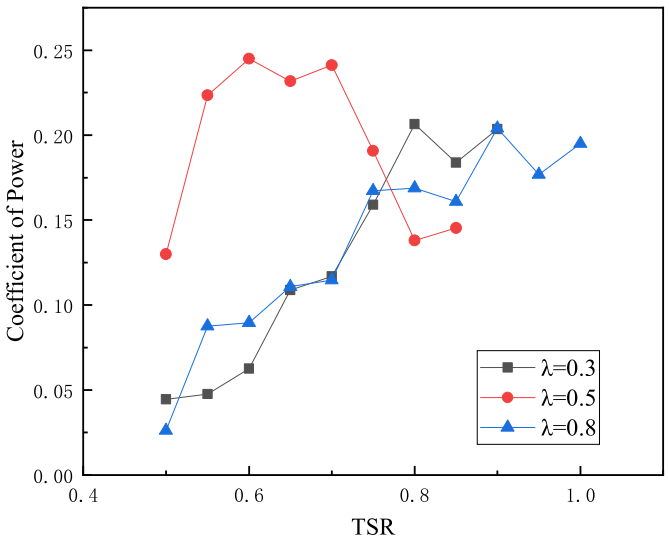

Fig. 12. Impeller coefficients power corresponding to different λ values and different TSRs for impellers with four blades.

decrease c_p, and the larger the value of λ is, the faster the decrease in c_p will be. Impellers with smaller λ have higher performance at high water flow speeds, and impellers with larger λ have higher performance at low water flow speeds.

(4) Impellers with different λ values also exhibit different trends with the change in TSR. When $\lambda = 0.3$ and 0.8, c_p increases with the increase in impeller TSR. Although c_p is stable at 0.2, when $\lambda = 0.8$, c_p of the impeller reaches a maximum at low water flow speed, and, when $\lambda = 0.3$, c_p reaches a maximum at high water flow speed. When $\lambda = 0.5$, c_p first increases and then decreases with the increase in TSR, and it is the best in the TSR range of 0.55–0.7, which is higher than that of the impellers with $\lambda = 0.3$ and 0.8.

Funding

This research was funded by the Guangdong Provincial Science and Technology Plan Project (Grant Nos. 2017A050506054 and 2017A010104011) and the Zhanjiang City Science and Technology Plan Project (Grant No. 2018A02013).

CRediT authorship contribution statement

Zhen-hai Wu: Numerical simulation, data processing and manuscript writing. **Qing Xu:** Scheme design, numerical simulation. **Changming Ling:** Conceptualization, method. **Chang-qin Wu:** experimental research.

Declaration of competing interest

The authors declare that they have no known competing financial interests or personal relationships that could have appeared to influence the work reported in this paper.

References

Abdelsalam, A.M., Kotb, M.A., Yousef, K., Sakr, I.M., 2021. Performance study on a modified hybrid wind turbine with twisted Savonius blades. Energy Convers. Manag. 241, 114317 https://doi.org/10.1016/j.enconman.2021.114317.

Abdolkarim, S.P., Amir, F.N., Franco, M., 2020. Investigation of deflector geometry and turbine aspect ratio effect on 3D modified in-pipe hydro Savonius turbine: parametric study. Renew. Energy 148 (C), 44–59. https://doi.org/10.1016/j.renene.2019.12.002.

Abdul, G.M., Suprayogi, D., Yaakob, O., Tawi, K., 2013. Experimental studies on savonius-type vertical Axis turbine for low marine current velocity. Int. J. Eng. 26 (1), 91–98. https://doi.org/10.5829/idosi.ije.2013.26.01a.12.

Ahmed, E., 2016. Prediction of regular wave loads on a fixed offshore oscillating water column-wave energy converter using CFD. J. Ocean Eng. Sci. 1 (4), 268–283. https://doi.org/10.1016/j.joes.2016.08.001.

Amy, H.I.L., Chen, H.H., Kang, H.Y., 2017. A conceptual model for prioritizing dam sites for tidal energy sources. Ocean Eng. 137, 38–47. https://doi.org/10.1016/j.oceaneng.2017.03.039.

Chen, J.H., Wang, X.C., Li, H., Jiang, C.H., Bao, L.J., 2020. Design of the blade under low flow velocity for horizontal Axis tidal current turbine. J. Mar. Sci. Eng. 8 (12), 989. https://doi.org/10.3390/jmse8120989.

El-Shahat, S.A., Li, G.J., Lai, F., Fu, L., 2020. Investigation of parameters affecting horizontal axis tidal current turbines modeling by blade element momentum theory. Ocean Eng. 202 (C), 107176. https://doi.org/10.1016/j.oceaneng.2020.107176.

Fei, Y.T., 2015. Error Theory and Data Processing. China Machine press, pp. 83–99.

Intizar, A.T., Madad, A.S., Tanweer, H., Khanji, H., Nayyar, H.M., Abdul, H.M., 2020. Investigation of duct augmented system effect on the overall performance of straight blade Darrieus hydrokinetic turbine. Renew. Energy 153 (C), 143–154. https://doi.org/10.1016/j.renene.2020.02.012.

Ion, P., Li, C., Ye, Z., Gao, W., 2013. Principle and Design of Vertical Axis Wind Turbine: Wind Turbine Design with Emphasis on Darrieus Concept. Shanghai Science and Technology Press, pp. 15–31.

Ling, C.M., Xu, Q., Li, J., Peng, L.M., Zhang, M.Y., 2019-10-25. A Semi-submersible Marine Energy Power Generation Device, CN2019105982610.

Li, W., Zhou, H.B., Liu, H.W., Lin, Y.G., Xu, Q.K., 2016. Review on the blade design technologies of tidal current turbine. Renew. Sustain. Energy Rev. 63, 414–422. https://doi.org/10.1016/j.rser.2016.05.017.

Ling, C.M., Zhang, M.Y., Li, R.S., Zhong, Y., Li, J., 2019-4-12. A Semi-submersible Marine Energy Power Generation Device: CN201811238057X.

Luo, X.Q., Zhu, G.J., Feng, J.J., 2014. Multi-point design optimization of hydrofoil for marine current turbine. J. Hydrodynamic. Ser B 26 (5), 807–817. https://doi.org/10.1016/S1001-6058(14)60089-5.

Maldar, N.R., Cheng, N.Y., Oguz, E., 2020. A review of the optimization studies for Savonius turbine considering hydrokinetic applications. Energy Convers. Manag. 226, 113495 https://doi.org/10.1016/j.enconman.2020.113495.

Madhan, P.K., Jeonghwa, S., Woochan, S., Shin, H.R., Abdus, S., 2019. Multi-fidelity optimization of blade thickness parameters for a horizontal axis tidal stream turbine. Renew. Energy 135, 277–287. https://doi.org/10.1016/j.renene.2018.12.023.

Menter, F.R., 1994. Two-equation eddy-viscosity turbulence models for engineering applications. AIAA J. 32 (8), 1598–1605. https://doi.org/10.2514/3.12149.

Mohammad, M., Ya J, S., Yong, H.X., 2012. Effects of near-wall grid spacing on SST-K-ω model using NREL Phase VI horizontal axis wind turbine. J. Wind Eng. Ind. Aerod. https://doi.org/10.1016/j.jweia.2012.03.032.

Patxi, G.N., Yusaku, K., 2019. Analysis of turbulence and extreme current velocity values in a tidal channel. J. Mar. Sci. Technol. 24 (3), 659–672. https://doi.org/10.1007/s00773-018-0601-z.

Ramin, A., Roozbeh, A., Seyed, S.R.K., Michal, P., Seyed, A.G., 2020. On the performance of small-scale horizontal Axis tidal current turbines. Part 1: one single turbine. Sustainability 12 (15), 1–25. https://doi.org/10.3390/su12155985.

Ramana, M.S.V., Kishore, K.S., 2013. Effect of different turbulence models on the numerical analysis of axial flow turbine stage of a typical turbofan engine. In: Proceedings of the ASME 2013 Gas Turbine India Conference. https://doi.org/10.1115/gtindia2013-3555. V001T02A004. ASME.

Salleh, M.B., Kamaruddin, N.M., Zulfaa, M.K., Bakar, E.A., 2021a. Experimental investigation on the characterization of self-starting capability of a 3-bladed Savonius hydrokinetic turbine using deflector plates. Ocean Eng. 228, 108950 https://doi.org/10.1016/j.oceaneng.2021.108950.

Salleh, M.B., Kamaruddin, N.M., Zulfaa, M.K., 2021b. The effects of a deflector on the self-starting speed and power performance of 2-bladed and 3-bladed Savonius rotors for hydrokinetic application. Energy Sustain. Develope. 61, 168–180. https://doi.org/10.1016/j.esd.2021.02.005.

Sufian, F.S., Ming, L., Brian, A.O., 2017. 3D modelling of impacts from waves on tidal turbine wake characteristics and energy output. Renew. Energy 114, 308–322. https://doi.org/10.1016/j.renene.2017.04.030.

Sun, J.J., Huang, D.G., 2020. Numerical investigation on aerodynamic performance improvement of vertical-axis tidal turbine with super-hydrophobic surface. Ocean Eng. 217, 107995 https://doi.org/10.1016/j.oceaneng.2020.107995.

Vimal, P., Ganapathi, B., Eldho, T.I., Prabhu, S.V., 2017. Influence of overlap ratio and aspect ratio on the performance of Savonius hydrokinetic turbine. Int. J. Energy Res. 41 (6), 829–844. https://doi.org/10.1002/er.3670.

Vogel, C.R., Taira, D.T., Carmo, B.S., Assi, G.R.S., Willden, R.H.J., Meneghini, J.R., 2019. Prospects for tidal stream energy in the UK and south America: a review of challenges and opportunities. Polytechnica: Innovat. Eng. Global Challenge. 2 (2), 97–109. https://doi.org/10.1007/s41050-019-00017-y.

Wang, B.Z., Hu, T.Y., Guo, Y., Zhang, Y.F., 2020. Research on pitch control strategies of horizontal Axis tidal current turbine. China Ocean Eng. 34 (4), 223–231. https://doi.org/10.1007/s13344-020-0021-9.

Wang, S.Y., Derek, B.I., Ma, L., Pourkashanian, Tao, Z., 2012. Turbulence modeling of deep dynamic stall at relatively low Reynolds number. J. Fluid Struct. 33, 191–209. https://doi.org/10.1016/j.jfluidstructs.2012.04.011.

Yao, J.J., Li, F.S., Chen, J.H., Yuan, Z., Mai, W.G., 2019. Parameter analysis of Savonius hydraulic turbine considering the effect of reducing flow velocity. Energies 13 (1), 24. https://doi.org/10.3390/en13010024.

Yuan, J.P., Mao, H.F., Pan, X.X., Jia, B.Z., Ji, R., 2020. Current situation and prospects of research on floating offshore wind turbines—based on the South China Sea area.

J. Guangdong Ocean University. 40 (5), 133–138. https://doi.org/10.3969/j.issn.1673-9159.2020.05.017.
Zhang, M.Y., 2019. Study on Cross-Interface Semi-submersible Ocean Current Energy Generation Method and Device (Master's Thesis. Guangdong Ocean University. https://kns.cnki.net/KCMS/detail/detail.aspx?dbname=CMFD202101&filename=1020445522.nh.
Zhao, G., Su, X.H., Cao, Y., Su, J.C., Liu, Y., 2016. Experiments on the hydrodynamic performance of horizontal axis tidal current turbine and desalination of sea water. Int. J. Energy Res. 40 (5), 600–609. https://doi.org/10.1002/er.3442.
Zhu, F.W., Ding, L., Huang, B., Bao, M., Liu, J.T., 2020. Blade design and optimization of a horizontal axis tidal turbine. Ocean Eng. 195 (C), 106652. https://doi.org/10.1016/j.oceaneng.2019.106652.